Journal of Electrical Engineering and Automation (ISSN: 2582-3051)
www.irojournals.com/iroeea/

Optimized Dual Loop Control in PV – based LVDC Microgrid With Hybrid Energy Storage for Enhanced Power Management

Roshini D.[1], Sowkarthika S.[2]

[1]PG Scholar, Power Electronics and Drives, Government College of Technology, Coimbatore, India

[2]Electrical & Electronics Engineering, Government College of Technology, Coimbatore, India

Email: [1]rosh.71772373203@gct.ac.in, [2]sowkarthika.s@gct.ac.in

Abstract

This study proposes a power management plan for an LVDC (Low-Voltage Direct Current) microgrid that is linked with solar energy and connected to a HESS (Hybrid Energy Storage System) that consists of a supercapacitor and battery. This study analyses the microgrid's performance with a focus on integrating hybrid energy storage devices to manage the unpredictable nature of renewable energy resources and load demands. The primary goals are creating a DC link voltage controller, building the battery and supercapacitor current controller, and activating a solar power generating unit using the Perturb and Observe MPPT algorithm. Additionally, a dual loop control strategy is created for the HESS. The power management method controls DC voltage and maintains power balance.

Keywords: LVDC Micro Grid, HESS, Battery, Super Capacitor, PV, Dual Loop Controller, P & O Algorithm, Power Management Scheme.

1. Introduction

Microgrids have emerged as a promising solution for integrating distributed energy resources (DERs) to enhance energy reliability and sustainability. These systems operate either

DOI: https://doi.org/10.36548/jeea.2025.1.005
Received: 18.03.2025, received in revised form: 12.04.2025, accepted: 27.04.2025, published: 07.04.2025

independently or in conjunction with the main grid, offering improved resilience against power disruptions. Among different microgrid configurations, DC microgrids are gaining traction due to their inherent efficiency, reduced conversion losses, and compatibility with modern electronic loads. To further enhance their stability and performance, hybrid energy storage systems (HESS), which combine batteries and supercapacitors, are increasingly being adopted. These storage systems play a vital role in regulating voltage fluctuations and improving energy management within the microgrid [1], [16]–[18].

Low-Voltage Direct Current (LVDC) microgrids offer significant advantages over conventional AC-based systems, such as simplified control, higher energy efficiency, and reduced power conversion stages. Their ability to integrate renewable energy sources like solar and wind makes them an ideal solution for sustainable energy distribution. Effective power management in LVDC microgrids is essential for ensuring stable voltage levels and efficient energy utilization. Advanced control strategies enable seamless coordination between different energy storage components, allowing the system to handle load variations and transient disturbances efficiently [4], [18], 19].

This study focuses on the implementation of an optimized power management scheme for a PV-based LVDC microgrid integrated with a hybrid energy storage system. The proposed approach aims to maintain stable DC bus voltage, balance power distribution, and enhance system reliability. By employing an autonomous control strategy, the system effectively manages the interaction between batteries and supercapacitors to mitigate power fluctuations and improve overall energy efficiency. The findings of this research contribute to the advancement of LVDC microgrid technologies, supporting their role in the transition toward resilient and sustainable power systems [7], [16], [19].

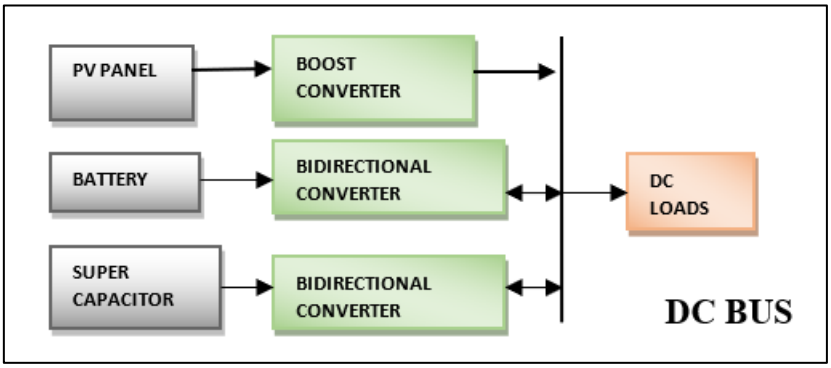

Figure 1. LVDC Microgrid Structure

The structure of an LVDC microgrid is shown on Figure. 1. PV panels need a DC/DC boost converter to connect to the DC bus. Supercapacitor (SC) and battery are connected to the DC bus via a bidirectional DC/DC converter. The DC loads are linked to the DC bus. 200 DC bus voltages are used in this work.

2. PV-HESS based LVDC Microgrid

An LVDC microgrid that uses solar power and HESS is depicted in Figure. 2 because its primary distributed energy resources (DERs) are linked to the DC bus through the use of suitable DC-DC converters.

The photovoltaic (PV) array and boost converter are integrated into a single DC bus in the solar power system. A lead-acid battery and a supercapacitor make up the hybrid energy storage system, which is linked to the DC bus for bidirectional DC/DC converters. Regardless of any imbalance between generation and demand, the HESS maintains a steady DC bus voltage and balances out power fluctuations brought on by SPG's (solar power generation) intermittent nature. Because of its unique power limitations, the battery is only meant to provide the average power requirement; in contrast the high-specific-power supercapacitor efficiently manages brief transients.

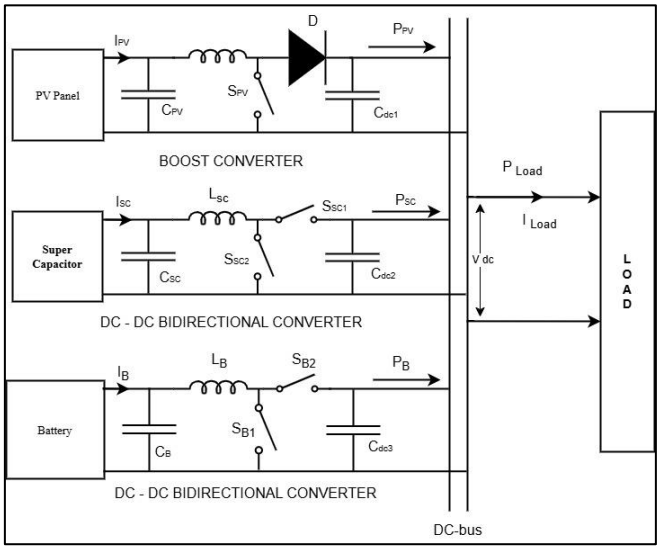

Figure 2. Circuit Diagram of LVDC Microgrid

2.1 Solar Power Generation

This is accomplished by attaching a DC/DC boost converter between the PV panel and the load, as illustrated in Figure. 2. By modifying the boost converter's current(Ipv), the solar power generation can efficiently extract the maximum power.

The value of inductance (L_{pv}) and capacitance (C_{pv}) in the low pass filter of a boost converter are determined to reduce ripple current and maintain a stable output voltage. The inductor is chosen to control current fluctuations, while the capacitor helps smooth out voltage variations, ensuring a steady DC output.

$$L_{pv} = \frac{V_{pv} * D_{pv}}{\Delta I_{pv} * F_s} \quad (1)$$

$$C_{pv} = \frac{V_{DC} * D_{pv}}{\Delta V_{DC} * F_s * R_L} \quad (2)$$

Where, $V_{DC,}$ $V_{pv,}$ $D_{pv,}$ F_s and R_L represent the DC bus voltage, PV voltage, duty cycle of the PV boost converter, switching frequency, load resistance respectively. PV inductance, dc link capacitance, PV capacitance values are L_{pv}= 2 mH, C_{DC} = 2860 μF, C_{pv} = 220 μF, $F_s = 10\ kHz$.

The perturb and observe-MPPT technique is employed to extract maximum power from the PV system. The program continuously adjust the operation point by changing the voltage and tracking the consequent power change. Through this procedure, the system is guaranteed to run at its peak efficiency in a range of sunlight circumstances.

2.2 Hybrid Energy Storage System(Hess)

Energy storage during times of excess generation and energy supply during times of high demand or inadequate renewable energy generation are the two primary tasks carried out by the battery. These functionalities are made possible by a bidirectional DC-DC converter, which serves as an interface between the battery and the DC bus. The bidirectional converter makes it easier for power to move smoothly throughout charging and discharging processes.

Bidirectional converters function as boost converters in discharging mode and as buck converters in charging mode.

The value of inductance (L_B) and capacitance (C_B) in the low pass filter of a bidirectional DC/DC converter are calculated as,

$$L_{B-BUCK} = \frac{V_b(1 - D_b)}{F_s * \Delta I_b} \quad (3)$$

$$L_{B-BOOST} = \frac{V_b * D_b}{F_s * \Delta I_b} \quad (4)$$

$$L_B = \max [L_{B-BOOST}: L_{B-BUCK}]$$

$$C_B = \frac{V_{DC} * D_B}{\Delta V_{DC} * F_s * R_L} \quad (5)$$

Where, $V_{DC,}\, V_B,\ D_B\ , F_s$ and R_L represent the DC bus voltage, Battery voltage, The battery bidirectional converter's duty cycle, load resistance respectively. Battery inductance, dc link capacitance, PV capacitance values are L_B= 2 mH, C_{DC} = 2860 μF, C_B = 220 μF, $F_s = 10\ kHz$. Inductor current ripple (ΔI_b) is limited 10% and DC bus voltage ripple (ΔV_{DC}) is limited 1%. Similarly, The value of inductance (L_{sc}) and capacitance (C_{sc}) in the low pass filter of a super capacitor bidirectional DC/DC converter are calculated.

3. Dual Loop Controller Design

Designing a stable DC link voltage controller for all operating conditions is essential in microgrid systems. This work utilizes a dual-loop control strategy, where the inner loop regulates the current for different sources, such as the PV system, battery, and super capacitor, while the outer loop maintains a stable DC link voltage. To simplify voltage controller design, the current control loops for the PV, battery, and super capacitor must have high bandwidth, ensuring fast dynamic response and effective power management.

3.1 Optimization of PV Current Control Loop

How a DC/DC converter connects to the DC bus with a solar panel is shown in Figure. 3(a). The PV current control loop is displayed in Figure. 3(b). Again factor H_{pv} is used to feed

the error amplifier the boost converter's input inductor current. Gating pulses for the switch are then produced by processing the PI controller's output using pulse-width modulation.

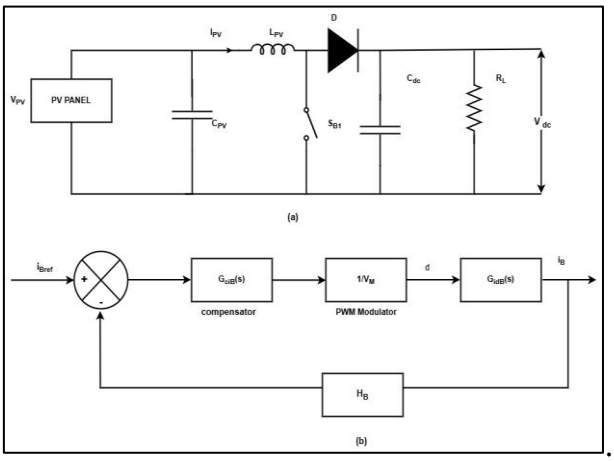

Figure 3. (a) PV Converter (b) PV Current Control Loop

The transfer function relates the i_{pv} and D_{pv} is expressed as follows

$$G_{\text{idp}}(s) = \frac{\hat{\imath}_p(s)}{\hat{d}_p(s)} = G_{\text{idp0}} \frac{1+\frac{s}{\omega_{\text{zip}}}}{1+\frac{s}{Q_p \omega_{0\text{p}}}+\frac{s^2}{{\omega_{0\text{p}}}^2}} \qquad (6)$$

Where,

$$\text{G}_{\text{idp0}} = \frac{2 * \text{v}_{\text{dc}}}{\text{R}_{\text{L}}(1-\text{D}_{\text{pv}})} = 51.20,\ \omega_{\text{zip}} = \frac{2}{\text{R}_{\text{L}}\text{C}_{\text{dc}}} = 35\,\text{rad/s}$$

$$\text{Q}_{\text{p}} = (1-\text{D}_{\text{pv}})\sqrt{\frac{\text{C}_{\text{dc}}}{\text{L}_{\text{pv}}}} = 15,\ \ \omega_{0\text{p}} = \frac{(1-\text{D}_{\text{pv}})}{\sqrt{\text{C}_{\text{dc}}\text{L}_{\text{pv}}}} = 261\,\text{rad/s}$$

Where,

$$V_{dc} = 200\,V, L_{pv} = 2\,mH, R_L = 20\ \Omega, \text{C}_{\text{dc}} = 2860\ \mu\text{F}, D_{pv} = 0.375.$$

The uncompensated loop gain $T_{up(S)} = \frac{H_p}{V_M} G_{idp}(s)$ (7)

Where, H_p=1 and V_M=1. The uncompensated loop gain exhibits a phase margin of 90° at 16 kHz. To improve dynamic and steady state performance F_{cpv} =2 kHz is selected as the ideal crossover frequency for the corrected loop gain.

$$G_{cip}(s) = G_{cip0}\frac{1+\frac{\omega_{zcip}}{s}}{1+\frac{s}{\omega_{pcip}}} \qquad (8)$$

$$\omega_{\text{zcip}} = 2\pi F_{\text{cpv}}/10 = 12566.37 \text{ rad/s}$$

$$\omega_{\text{pcip}} = 2\pi F_{\text{cpv}}*10 = 125663.7 \text{ rad/}s$$

The compensated loop gain

$$|T_{cp}| = |\frac{H_p}{V_M} * G_{cip}(s) * G_{idp}(s)| = 1 \qquad (9)$$

$$G_{ciB0} = \frac{H_B}{V_M} * \frac{2 * \pi * f_{cB} * L_B}{v_{dc}} = 0.1260 \qquad (10)$$

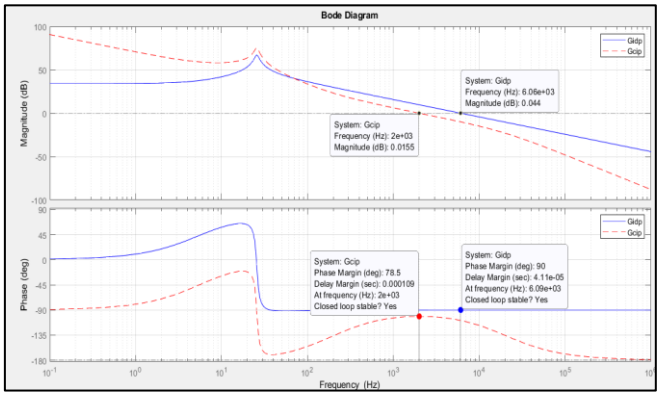

Figure 4. Bode Plot for the Current Control Loop of the PV Converter, both Uncompensated and Compensated

At 2 kHz, the adjusted loop gain has a 78.5° phase margin and an infinite gain margin. Consequently, the closed-loop current control of the PV attains a high bandwidth and is stable as shown in Figure 4.

3.2 Optimization of Battery Current Control Loop

Similar in design to the PV current controller is the battery current controller.$V_{dc} = 200\ V, L_B = 2\ mH, R_L = 20\ \Omega$, $C_{dc} = 2860\ \mu F, D_{pv} = 0.52$, $G_{idB0} = 86.80$, $Q_B = 11.5$, $\omega_{ziB} = 35\frac{\text{rad}}{\text{s}}$, $\omega_{0B} = 200\frac{\text{rad}}{\text{s}}$. The uncompensated loop gain has phase margin 90°at 15.9 kHz shown in Figure. 5. To enhance both dynamic and steady-state performance, a compensator is added. The corrected loop gain's crossover frequency is 5 kHz, $G_{ciB0} = 0.3142$. Figure. 5

displays the adjusted loop gain. At 5 kHz, the adjusted loop gain shows a 78.5° phase margin and an infinite gain margin.

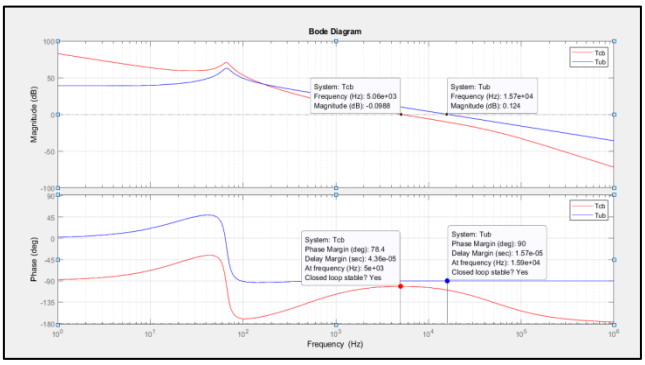

Figure 5. Bode Plot for the Current Control Loop of the Battery Converter, both Uncompensated and Compensated

3.3 Optimization of Supercapacitor Current Control Loop

The PV current controller and the supercapacitor current controller share a similar design.$V_{dc} = 200\,V, L_{sc} = 2\,mH, R_L = 20\ \Omega$, $C_{dc} = 2860\ \mu F, D_{sc} = 0.44$, $G_{idsc0} = 63.77$, $Q_{sc} = 13.4$, $\omega_{zisc} = 35\,\frac{rad}{s}$, $\omega_{0sc} = 234\,\frac{rad}{s}$

The uncompensated loop gain has phase margin 90° at 15.9 kHz shown in Figure. 5. A compensator is introduced to improve both dynamic and steady-state performance. The adjusted loop gain's crossover frequency is 6 kHz, $G_{cisc0} = 0.3760$. Figure. 6 displays the adjusted loop gain. At 6 kHz, the adjusted loop gain shows a 78.5° phase margin and an infinite gain margin.

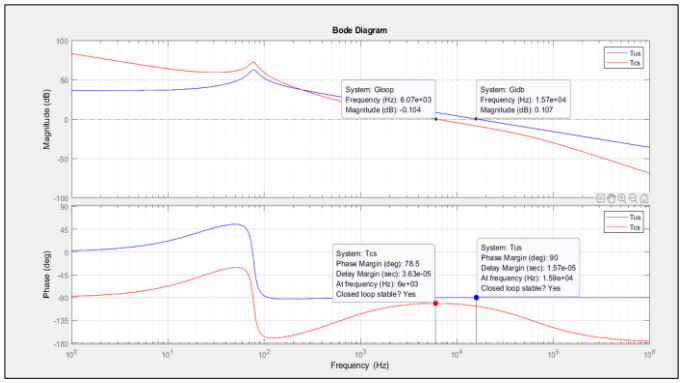

Figure 6. Bode Plot for the Current Control Loop of the Super Capacitor Converter, Both Uncompensated and Compensated

3.4 Optimization DC Link Voltage Control Loop

$$V_{dc} = 200\ \text{V}, L_S = L_B = 2\ \text{mH}, R_L = 200\ \Omega, C_{dc} = 2860\ \mu\text{F}, D_S = 0.44$$

$$D_B = 0.52, H_B = H_v = 1 G_{idB0} = \frac{H_v D_B{}' R_L}{2H_B} = 4.8, G_{idS0} = \frac{H_v D_S{}' R_L}{2H_S} = 5.6, G_f = \frac{1}{1 + 0.5s}$$

The uncompensated loop gain of the DC link voltage control loop.

$$T_{uv}(s) = H_v\left[\frac{G_f(s) G_{viB}(s)}{H_B} + \frac{(1 - G_f(s)) G_{vis}(s)}{H_S}\right] \qquad (11)$$

The uncompensated loop gain is shown in Figure. 6 with a gain margin of 31.3 dB and a phase margin of 90.9° at 31.2 Hz. A compensator $G_{cv}(s)$ is designed.

$$G_{cv}(s) = G_{cv0}\left[1 + \frac{\omega_{zcv}}{s}\right] \qquad (12)$$

$$\omega_{zcv} = 2\pi f_{cv}/5 = 46.5 rad/s \qquad (13)$$

$$G_{cv0} = \frac{1}{|T_{uv}(j\omega_{cv})|} \qquad (14)$$

Figure. 7 displays the DC link voltage compensated loop gain. It shows a gain margin of 22.8 dB at infinite Hz and a phase margin of 79.3° at 37.2 Hz. This illustrates the stability of the voltage control loop with the battery and super capacitor converter in the inner current control loop.

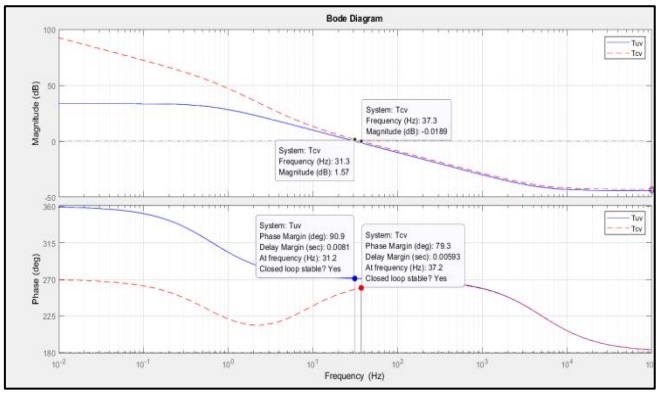

Figure 7. Bode Plot for the DC Link Voltage Control Loop Both Uncompensated and Compensated

4. Power Management Scheme of LVDC Microgrid

The power management scheme's block diagram is shown in Figure. 8. This plan guarantees that the super capacitor will handle fast transients and the battery will handle slow ones. The DC link voltage is then transferred through the PI compensator after being compared to the reference voltage ($V_{dc}{}^{*}$).

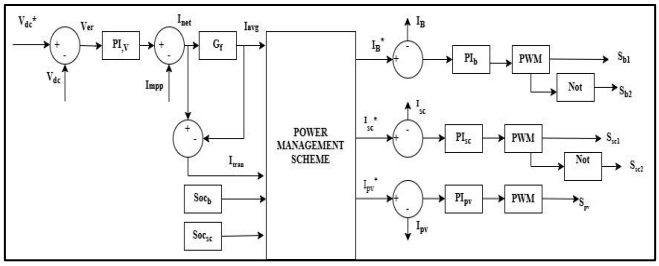

Figure 8. Block Diagram of Power Management Scheme

The output current of PI, when compared to the maximum power point current (I_{mpp}), determines the I_{net}. If (I_{net}) is positive, it indicates a generation is in deficit mode, while a negative I_{net} signifies an excess generation mode.

$$I_{net} = \left(V_{err} * \left(K_{pv} + \frac{K_{iv}}{S}\right)\right) - I_{mpp} \qquad (15)$$

As shown in Figure. 7, a low-pass filter G_{lpf} separates the entire current supplied by the hybrid energy storage system into average and transient power components. The reference current ($I_B{}^{*}$) for the battery current control loop is supplied by the average power component.

$$I_{avg} = I_{net}(s) * G_{lpf} = I_B{}^{*} \qquad (16)$$

The supercapacitor current control loop's reference current ($I_{sc}{}^{*}$).

$$I_{sc}{}^{*} = I_{net}(s) - I_B{}^{*} \qquad (17)$$

PI controllers evaluate the error signals that emerge from comparing the reference currents for the supercapacitor and battery with the actual currents in order to calculate the appropriate duty ratios (d_{SC} & d_B).

$$d_b = \left(K_{p,B} + \frac{K_{i,B}}{s}\right)(I_B{}^{*} - I_B) \qquad (18)$$

$$d_{sc} = \left(K_{p,sc} + \frac{K_{i,sc}}{s}\right)(I_{sc}{}^{*} - I_{sc}) \qquad (19)$$

The purpose of the Power Management Scheme (PMS) is to provide the best possible power balance between the load and maintain the constant DC-bus voltage and the PV Generating Unit while efficiently controlling the charging and discharging of the HESS.

LVDC microgrid operates at 2 types of modes one is Deficit generation mode and another one is Excess Generation mode.

4.1 Excess Generation Mode

- $SOC_B < SOC_{B.H}\ and\ SOC_{SC} < SOC_{SC.H}$
- $SOC_B < SOC_{B.H}\ and\ SOC_{SC} > SOC_{SC.H}$
- $SOC_B > SOC_{B.H}\ and\ SOC_{SC} < SOC_{SC.H}$
- $SOC_B > SOC_{B.H}\ and\ SOC_{SC} > SOC_{SC.H}$

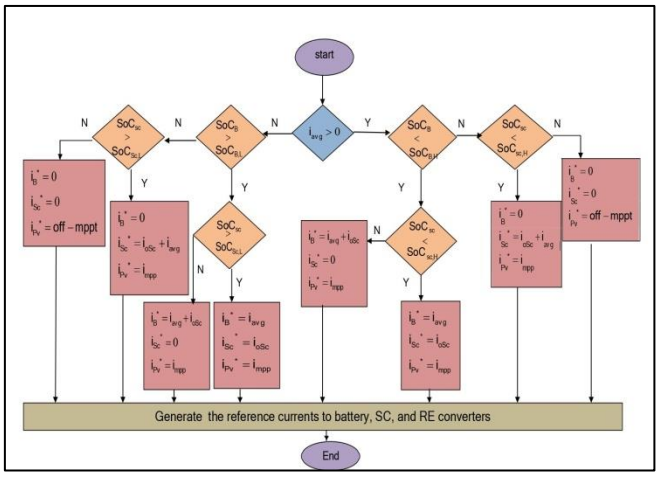

Figure 9. Flowchart of power Management Scheme

Mode 1: $SOC_B < SOC_{B.H}\ and\ SOC_{SC} < SOC_{SC.H}$

The battery handles average power. The supercapacitor absorbs transient power. To extract the most power, PV operates in MPPT mode.

$$i_B{}^{*} = i_{avg}, i_{Sc}{}^{*} = i_{oSc}, i_{Pv}{}^{*} = i_{mpp} \qquad (20)$$

Mode 2: $SOC_B < SOC_{B.H}\ and\ SOC_{SC} > SOC_{SC.H}$

Battery can charge the average power and manage the transient power. Supercapacitor cannot charge. To extract the most power, PV operates in MPPT mode.

$$i_B{}^* = i_{avg} + i_{oSc}, i_{Sc}{}^* = 0, i_{Pv}{}^* = i_{mpp} \quad (21)$$

Mode 3: $SOC_B > SOC_{B.H}\ and\ SOC_{SC} < SOC_{SC.H}$

Battery is idle. Supercapacitor can charge the transient power and manage the steady state power. To extract the most power, PV operates in MPPT mode.

$$i_B{}^* = 0, i_{Sc}{}^* = i_{avg} + i_{oSc}, i_{Pv}{}^* = i_{mpp} \quad (22)$$

Mode 4: $SOC_B > SOC_{B.H}\ and\ SOC_{SC} > SOC_{SC.H}$

Battery and Supercapacitor fully charged. PV operates at off-MPPT mode. The SC and battery can no longer absorb power and are left in active. Both SC & Battery is zero. The battery is shielded from overcharging by this action.

$$i_B{}^* = 0, i_{Sc}{}^* = 0, i_{Pv}{}^* = off - mppt \quad (23)$$

4.2. Deficit Generation Mode

- $SOC_B > SOC_{B.L}\ and\ SOC_{SC} > SOC_{SC.H}$
- $SOC_B > SOC_{B.L} and SOC_{SC} < SOC_{SC.L}$
- $SOC_B < SOC_{B.L} and SOC_{SC} > SOC_{SC.L}$
- $SOC_B \leq SOC_{B.L} and SOC_{SC} \leq SOC_{SC.L}$

Mode 5: $SOC_B > SOC_{B.L}\ and\ SOC_{SC} > SOC_{SC.H}$

The average power is provided by batteries. While the transient power is provided by a supercapacitor. To extract the most power. PV operates in MPPT mode.

$$i_B{}^* = i_{avg}, i_{Sc}{}^* = i_{oSc}, i_{Pv}{}^* = i_{mpp} \quad (24)$$

Mode 6: $SOC_B > SOC_{B.L} and SOC_{SC} < SOC_{SC.L}$

Battery can supply the average power and also manage the transient power. While supercapacitor cannot supply transient power. To extract the most power. PV operates in MPPT mode.

$$i_B{}^* = i_{avg} + i_{oSc}, i_{Sc}{}^* = 0, i_{Pv}{}^* = i_{mpp} \quad (25)$$

Mode 7: $SOC_B < SOC_{B.L} and SOC_{SC} > SOC_{SC.L}$

The average power cannot be supplied by a battery. Supercapacitors, on the other hand, can provide average and transient power. MPPT is used by the PV system to maximize power extraction.

$$i_B{}^* = 0, i_{Sc}{}^* = i_{oSc} + i_{avg}, i_{Pv}{}^* = i_{mpp} \quad (26)$$

Mode 8: $SOC_B \leq SOC_{B.L} and SOC_{SC} \leq SOC_{SC.L}$

The battery and supercapacitor are idle and unable to supply power. PV operates at off-MPPT mode. Both SC& Battery is zero. By doing this, the battery is shielded from deep discharge.

$$i_B{}^* = 0, \mathrm{i_{Sc}}{}^* = 0, \mathrm{i_{Pv}}{}^* = i_{\mathrm{mpp}} \quad (27)$$

5. Results and Discussion

Mode1: t=0 to 1.65 S: The average power is charged by the battery. Transient power is absorbed by the supercapacitor using the net reference current. To maximize power generation, the photovoltaic system uses the MPPT technology. The solar power generation unit operates under an irradiation of 1000 W/m². A constant 200 V DC link voltage and a 10 A load current were maintained. An under shoot occurred when the mode and irradiation were changed. This is evident from Figure. 10.

Mode 2: t=1.65 to 3 S: Using the net reference current, the battery charges the average power. Transient power cannot be absorbed by the supercapacitor. The photovoltaic system operates using the MPPT technique to optimize power generation. The solar power generation unit operates under an irradiation of 800 W/m². A constant 200 V DC link voltage and a 10 A load current were maintained. An undershoot occurred when the mode and irradiation were changed. This is evident from Figure. 10.

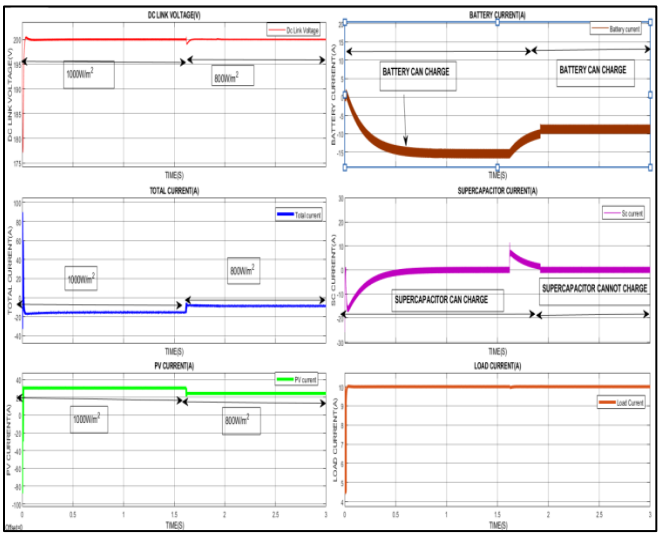

Figure 10. Output Waveform of Excess Generation Mode ($mode$:1 $B<B_H and Sc<Sc_H$), ($mode$:2 $B < B_H and\ Sc > Sc_H$) in DC Link Voltage, Total Current, PV Current, Battery Current, Supercapacitor Current

Table 1. LVDC Microgrid Parameter

DC bus voltage=200 V, RL=20 Ω, Cdc=2860 µF
PV Parameter
Series string:4, Parallel String:3 Lpv = 2 mH, Cpv=220 µF, Voc=36.8 V, Isc=8.51 A, Vmp=29.45 V, Imp=7.81 A
Battery Parameter
LB=2 mH, CB=220 µF, Battery Ah=26 Ah, Terminal Voltage=96 V
Super capacitor Parameter
Lsc=2 mH, Csc=220 µF, capacitance =58 F, Rated Voltage=96 V and current=19 A

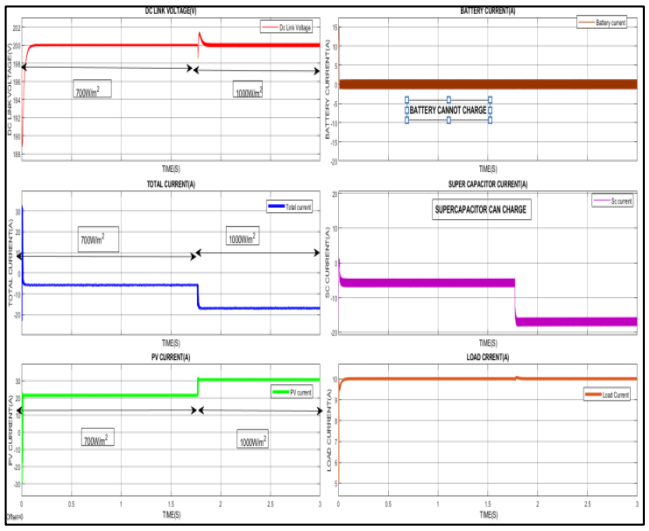

Figure 11. Output Waveform of Excess Generation Mode($mode$:3B>$B_H$andSc<ScH) in DC Link Voltage, Total Current, PV Current, Battery Current, Supercapacitor Current

Mode 3: 0 to 3 S: The battery cannot charge the average power. The supercapacitor can absorb transient power with the net reference current. To maximize power generation, the solar system uses the MPPT technology. The solar power generation unit experiences an irradiation of 700 W/m²from t=0 and 1.75 s, and 1000 W/m² from t=1.75 and 3 seconds. A constant 200 V DC link voltage and a 10 A load current were maintained. An undershoot occurred when the mode and irradiation were changed. This is evident from Figure. 11.

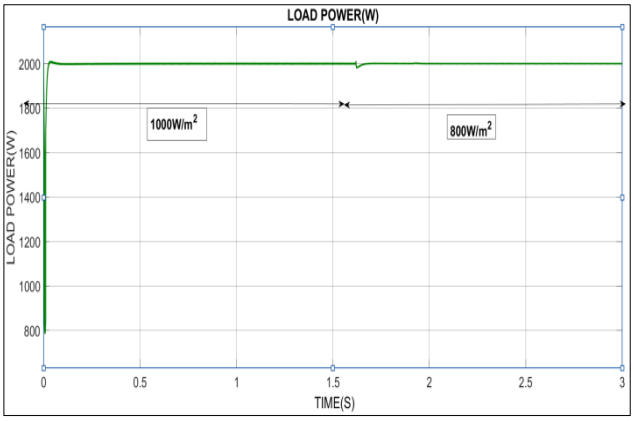

Figure 12. Load Power for Excess Generation Mode

Figure.12 illustrates that in excess generation mode, the power management scheme maintains a constant output of 2000 W.

Mode 5: t=0 to 2.6 S:While the supercapacitor provides transient power based on the net reference current, the battery provides the load with average power. To maximize power generation, the solar system uses the MPPT technology. The solar power generation unit experiences an irradiation of 500 W/m². A constant 200 V DC link voltage and a 10 A load current were maintained. An undershoot occurred when the mode and irradiation were changed. This is evident from Figure. 13.

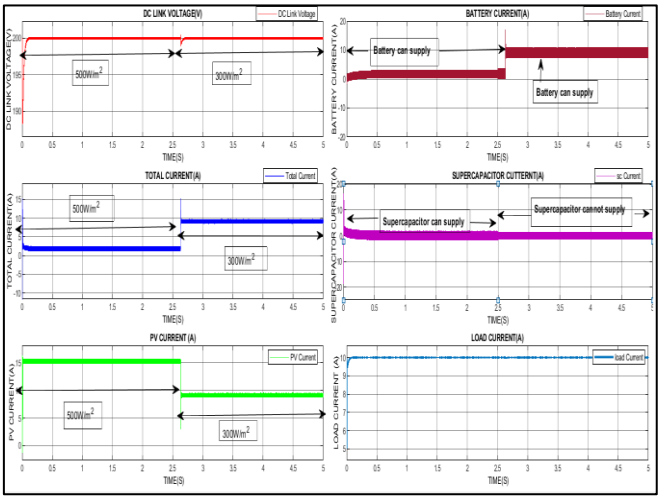

Figure 13. Output Waveform of Deficit Generation Mode in ($mode$:1 $B>B_L and Sc>Sc_L$), ($mode$:2 $B > B_L and\ Sc< Sc_L$) DC LINK VOLTAGE, Total Current, PV Current, Battery Current, Supercapacitor Current

Mode 6: t=2.6 to 5 S: While the supercapacitor is unable to deliver transient power with the net reference current, the battery provides the load with average power. In this system, the battery also manages the transient power. To maximize power generation, the solar system uses the MPPT technology. The solar power generation unit experiences an irradiation of 300 W/m². A constant 200 V DC link voltage and a 10 A load current were maintained. An undershoot occurred when the mode and irradiation were changed. This is evident from Figure. 13.

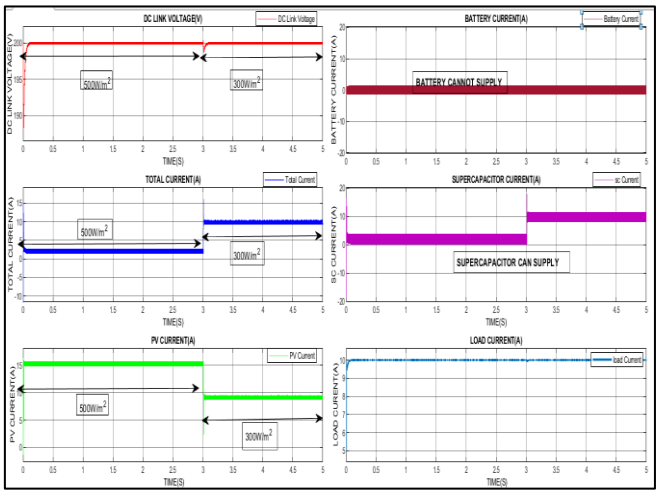

Figure 14. Output Waveform of Deficit Generation Mode ($mode$:3B<$B_H and Sc$>Sc_H) in DC Link Voltage, Total Current, PV Current, Battery Current, Super Capacitor Current

Mode 7: t=0 to 5 S:While the super capacitor manages the average power and supplies transient power with the net reference current, the load cannot receive the average power from the battery.. The PV operates at MPPT to maximize power extraction. The solar power generation unit experiences an irradiation of 500W/m² from t=0 and 3 S, and 300 W/m² from t=3 and 5 S. A constant 200 V DC link voltage and a 10 A load current were maintained. An undershoot occurred when the mode and irradiation were changed. This is evident from Figure. 14.

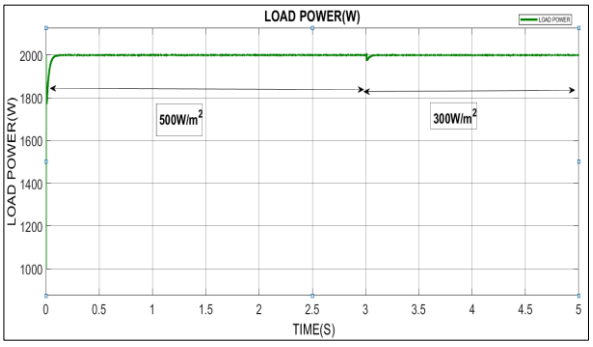

Figure 15. Load Power for Deficit Generation Mode

Figure. 15 illustrates that in deficit generation mode, the power management scheme maintains a constant output of 2000 W.

6. Conclusion

For a PV-powered LVDC (Low-Voltage Direct Current) microgrid with a HESS(Hybrid Energy Storage System) that combines a battery and supercapacitor, a dynamic power management strategy is recommended. This plan ensures steady operation and effective energy management by addressing the unpredictability of renewable energy output and varying load needs. Using a Perturb and Observe MPPT algorithm for solar power generation in combination with controllers designed for the battery and supercapacitor increases system efficiency. Furthermore, the dual-loop control strategy preserves power balance and successfully stabilizes the DC bus voltage. Future research can concentrate on enhancing the hybrid energy storage system's performance through the use of sophisticated control algorithms and prediction models. Furthermore, adding more renewable energy sources like wind or grid connectivity—could increase the system's resilience and dependability. Exploring real-time adaptive control methods and implementing the system in a practical, real-world environment will also be valuable to assess its scalability and performance under various operating conditions.

References

[1] S. Kotra, M. K. Mishra “Design and stability analysis of DC microgrid with hybrid energy storage system”, IEEE Transactions on sustainable energy, vol. 10, no. 3, 3July 2019.

[2] D. Chen, L. Xu, and L. Yao, “Dc voltage variation based autonomous control of dc microgrids,” IEEE Trans. Power Del., vol. 28, no. 2, April 2013.

[3] Q. Xu, J. Xiao, X. Hu, P. Wang, and M. Y. Lee, “A decentralized power management strategy for hybrid energy storage system with autonomous bus voltage restoration and state-of-charge recovery,” IEEE Trans. on Ind. Electron., vol. 64, no. 9, Sept 2017.

[4] S. Kotra and M. K. Mishra, “A supervisory power management system for a hybrid microgrid with hess,” IEEE Transactions on Industrial Electronics, vol. 64, no. 5, May 2017.

[5] A. Nisar and M. S. Thomas, “Comprehensive control for microgrid autonomous operation with demand response,” IEEE Trans. on Smart Grid, vol. 8, no. 5, Sept 2017.

[6] B. Liu, F. Zhuo, Y. Zhu, and H. Yi, “System operation and energy management of a renewable energy-based dc micro-grid,” IEEE Trans. on Smart Grid, vol. 6, no. 3, May 2015.

[7] K. Shenai, A. Jhunjhunwala, and P. Kaur, “Electrifying india: Using solar dc microgrids,” IEEE Power Electronics Magazine, vol. 3, no. 4, Dec 2016.

[8] P. K. Behera and M. Pattnaik, “Power management of a laboratory scale wind- PV-battery based LVDC microgrid,” in Proc. IEEE IAS Glob. Conf. Emerg. Technol., 2022,

[9] D. Salomonsson, L. Soder, and A. Sannino, “An adaptive control system for a DC microgrid for data centers,” in Proc. IEEE Ind. Appl. Annu. Meeting, 2007,

[10] L. Wang, C.-Y. Lin, H.-Y. Wu, and A. V. Prokhorov, “Stability analysis of a microgrid system with a hybrid off shore wind and ocean energy farm fed to a power grid through an HVDC link,” IEEE Trans. Ind. Appl., vol. 54, no. 3, May/Jun. 2018.

[11] A. Jhunjhunwala, A. Lolla, and P. Kaur, “Solar-DC microgrid for indian homes: A transforming power scenario,” IEEE Electrific. Mag.,vol.4, no. 2, Jun. 2016.

[12] S. A. G. K. Abadi, J. Choi, and A. Bidram, “A method for charging electric vehicles with battery-supercapacitor hybrid energy storage systems to improve voltage quality and battery lifetime in islanded building-level DC microgrids,” IEEE Trans. Sustain. Energy, vol. 14, no. 3, Jul. 2023.

[13] W. Jing, C. H. Lai, S. H. W. Wong, and M. L. D. Wong, “Battery supercapacitor hybrid energy storage system in standalone DC microgrids: A review, ” IET Renewable Power Gener., vol. 11, no. 4,2017.

[14] T. S. Babu, K. R. Vasudevan, V. K. Ramachandaramurthy, S. B. Sani, S. Chemud, and R. M. Lajim, “A comprehensive review of hybrid energy storage systems: Converter topologies, control strategies and future prospects,” IEEE Access, vol. 8, 2020

[15] K. A. Khan, A. Atif, and M. Khalid, “Hybrid battery-supercapacitor energy storage for enhanced voltage stability in DC microgrids using autonomous control strategy,” in Emerging Trends in Energy Storage Systems and Industrial Applications. Amsterdam, Netherlands: Elsevier, 2023.

[16] S. Hajiaghasi, A. Salemnia, and M. Hamzeh, “Hybrid energy storage system for microgrids applications: A review,” J. Energy Storage, vol. 21, 2019.

[17] S. Kotra, M. K. Mishra and N. P. Chaithanya, "Design and small signal analysis of DC microgrid with hybrid energy storage system," 2017 IEEE PES Asia-Pacific Power and Energy Engineering Conference (APPEEC), Bangalore, India, 2017.

[18] S. K. Kollimalla, M. K. Mishra and N. L. Narasamma, "Design and Analysis of Novel Control Strategy for Battery and Supercapacitor Storage System," in *IEEE* Transactions on Sustainable Energy, vol. 5, no. 4, Oct. 2014.

[19] P. K. Behera and M. Pattnaik, "Supervisory Power Management Scheme of a Laboratory Scale Wind-PV Based LVDC Microgrid Integrated With Hybrid Energy Storage System," in IEEE Transactions on Industry Applications, vol. 60, no. 3, May-June 2024.